Results in Physics 69 (2025) 108132

Contents lists available at ScienceDirect

Results in Physics

journal homepage: www.elsevier.com/locate/rinp

X-ray phase contrast imaging and diffraction in the laser-heated diamond anvil cell: A case study on the high-pressure melting of Pt

Emma Ehrenreich-Petersen [a,*], Bernhard Massani [b], Thea Engler [c], Olivia S. Pardo [d], Konstantin Glazyrin [a], Nico Giordano [a], Johannes Hagemann [c], Daniel Sneed [d], Timofey Fedotenko [a], Daniel J. Campbell [d], Mario Wendt [a], Sergej Wenz [a], Christian G. Schroer [c,e,f], Mathias Trabs [g], R.Stewart McWilliams [b], Hanns-Peter Liermann [a], Zsolt Jenei [d], Earl F. O'Bannon [d]

[a] Deutsches Elektronen-Synchrotron DESY, Notkestr. 85, 22607 Hamburg, Germany
[b] School of Physics and Astronomy and Centre for Science at Extreme Conditions, University of Edinburgh, Edinburgh EH9 3FD, United Kingdom
[c] Center for X-ray and Nano Science CXNS, Deutsches Elektronen-Synchrotron DESY, Notkestr. 85, 22607 Hamburg, Germany
[d] Physics Division, Physical and Life Sciences Directorate, Lawrence Livermore National Laboratory, Livermore, CA 94550, USA
[e] Department Physik, Universität Hamburg, Luruper Chaussee 149, 22761 Hamburg, Germany
[f] Helmholtz Imaging, Deutsches Elektronen-Synchrotron DESY, Notkestr. 85, 22607 Hamburg, Germany
[g] Institut für Stochastik, Karlsruher Institut für Technologie, Englerstr. 2, Karlsruhe 76131, Germany

ARTICLE INFO

Keywords:
X-ray diffraction
Synchrotrons
Laser-heated diamond anvil cell
Phase contrast imaging
Melting
High pressure

ABSTRACT

Melting temperatures of materials at high-pressure are one of the key physical properties that can be measured. However, large discrepancies in high-pressure melt lines exist between different experimental and theoretical approaches. In this paper, we present a novel approach for melting determination at high pressure where time-resolved synchrotron X-ray phase contrast imaging is used to observe the solid to liquid phase transition in laser heated samples in the diamond anvil cell along with simultaneous X-ray diffraction. Optical radiometric temperature measurements are correlated with the observed phase boundaries determined from X-ray phase contrast images and structural information from X-ray diffraction patterns to determine the melting temperature. We benchmarked this new technique with experiments on the high-pressure melting of platinum (Pt). Our new Pt melting results are compared with several recent studies on the high pressure melt line of Pt which utilized different techniques to determine melting. The technique can readily be applied to other materials and offers great potential for the determination of accurate and precise melting temperatures.

Introduction

Melting temperature is a fundamental physical property of many materials, be it an element or compound. Melting at high-pressures and temperatures has been of significant interest to both the geophysics and materials science community, with melting temperatures of iron (Fe), for example, playing a pivotal role in understanding the dynamics and temperature structure of the Earth and other planetary bodies. However, severe discrepancies in melting conditions measured in high pressure, high temperature experiments (using both static and dynamic compression) as well as large discrepancies from theoretical calculations have persisted for decades in Fe [1–3], as well as in other archetypal metals such as Pt [4–6]. In the diamond anvil cell (DAC) a wide range of techniques have now been deployed to detect melting in materials at static high pressure, typically in combination with laser heating, and at least some of the proposed origins for these discrepancies include variations in the techniques used to detect melting. Some of the techniques to detect melting include detection of flickering of the optically imaged hot spot [7], the laser speckle technique for observation of movement [8,9], X-ray transmission microscopy [10], laser power-temperature plateaus [2,4], diffuse X-ray scattering from the melt [3,4], changes in resistivity and reflectivity [11,12], flash laser-heating combined with scanning electron microscopy and/or focused ion beam milling [13], X-ray absorption spectroscopy [14], Mössbauer spectroscopy [15], and

* Corresponding author.
E-mail address: emma.ehrenreich-petersen@desy.de (E. Ehrenreich-Petersen).

https://doi.org/10.1016/j.rinp.2025.108132
Received 19 December 2024; Received in revised form 15 January 2025; Accepted 26 January 2025
Available online 27 January 2025

detection of latent heat [5]. The type of the heating method that is used (e.g. resistive vs laser heating) [2,5] will have its own associated sample temperature variations [2], and systematic uncertainties associated with the temperature measurement technique or apparatus (e.g. pyrometry, thermocouples) could also dramatically influence the apparent melting conditions. This is especially true when considering that each melt diagnostic can have a unique relationship to temperature profiles; for example, in metals under laser heating, temperatures are measured on the directly-heated surfaces, with reduced temperature in the sample interior, so measurement of surface melting (such as laser-speckle) could obtain different apparent melting points than those measuring bulk melting (such as X-ray diffraction (XRD)). Moreover, prolonged heating can be associated with large-scale contamination of samples that could physically alter the melting temperatures [1], whilst solid-state microstructural changes at high temperature could also play a role in detecting melt [3,16]. Clearly, strategies to unambiguously detect melt and assign its temperature at high pressure are still necessary.

It was previously shown that a combination of X-ray phase contrast imaging (XPCI) and XRD can be used in the dynamic diamond anvil cell (dDAC) to investigate pressure induced phase changes in both optically transparent and opaque samples during isothermal compression [17]. Due to the strong contrast between boundaries of materials with different electron densities, this approach is ideal for imaging small features like a melt pool that is generated during laser heating.

In this paper, we describe a new experimental platform where we combine infrared laser heating with the simultaneous XPCI and powder XRD experimental platform described in Ref. [17]. This new experimental platform has been implemented at the laser heating experiment station at the Extreme Conditions Beamline (ECB), P02.2, at PETRA III, DESY [18]. This setup is supported by an improved illumination correction for the XPCI data, i.e. better flat-field corrected data compared to earlier reports, which provides excellent images for the detection of melting. To demonstrate the validity of this technique we report the findings of a comprehensive study on the melting temperature of Pt performed under high static pressures in the laser heated diamond anvil cell (LH-DAC). Pt has a wide range of important applications because of its chemical inertness and stability at extreme pressure and temperature conditions enabling its use as a pressure standard and laser-absorber for high pressure experiments [19,20].

The high-pressure melt line of Pt was determined with this new platform up to 50 GPa with temperatures reaching more than 3,000 K. We describe the technical details and the feasibility of this method, while critically discussing the obtained results and their significance. We anticipate that this study – and the results within – will stimulate research using the combined approach of XPCI, XRD, and laser heating to investigate the high pressure melting of a range of materials.

Materials and methods

Experimental setup

The experimental configuration for simultaneous XPCI and XRD was described in detail in Ref. [17]. Below we explain the changes enabling the implementation of this setup at the laser-heating experimental station at P02.2. This laser-heating setup has been described elsewhere [21] and the reader is referred to the existing literature for a review of the LH-DAC technique [22,23].

Propagation-based XPCI utilizing the partially coherent synchrotron-radiation source was performed in the divergent beam downstream (towards the detectors; after the sample stack) of the focus created through beryllium compound refractive lenses (CRLs) as described in Ref. [17]. With 49 CRLs (beam size of ~80 × ~80 μm^2) with a distance from the middle of the CRLs to the sample of 1350 mm, this corresponds (theoretically) to the focus being at 974 mm away from the CRLs and therefore a distance from the focus to the sample of 376 mm. It is currently not possible to experimentally measure the distance from the CRLs to the focus, and hence the focus to the sample, and we rely on the given theoretical numbers. The X-ray energy was tuned to 25.37 keV (0.4887 Å) for all pressure points except the one at 32.5(5) GPa, for which the energy was 25.56 keV (0.4851 Å). The incident wave front, modified by the complex refractive index of the sample, is measured by an indirect detection scheme using a cerium-doped lutetium aluminum garnet (LuAG:Ce) scintillator (10 μm in thickness), which is imaged by an X-ray microscope onto a PCO Edge 4.2 camera. However, in contrast to the earlier report [17], the imaging microscope and scintillator are here placed behind the two GaAs LAMBDA 2M XRD detectors instead of being in front of them. The XRD detector is placed ~270 mm behind the sample, whereas the scintillator for imaging is placed ~500 mm behind the sample. This provides a larger scattering angle (2θ) coverage of the XRD signal on the two LAMBDA 2M detectors compared to the configuration described in Ref. [17] (dDAC-XPCI-XRD), while maintaining a propagation distance for XPCI that does not impact the quality of the images from that observed in Ref. [17].

The triggering system used in this experiment is outlined in Fig. 1(a) and (b). This triggering setup utilizes the internal triggering mode of the PCO Edge 4.2 and the 12 bit mode of the LAMBDA detectors. Note, that the triggering scheme does not include the optical spectroscopy for temperature measurements as this was triggered separately in the present study; in a later implementation of this setup, the i-Star intensified CCD on the spectrometer [21] was also triggered with the PCO and LAMBDA detectors. The new configuration, termed LH-XPCI-XRD, is depicted in Fig. 1(c).

Samples

Samples were loaded in standard symmetric piston-cylinder type DACs. The gasket material in all cases was rhenium which was pre-indented to ~30 μm. The hole in the gaskets was approximately half the size of the culet of the diamonds used. For most cases, a 5 μm thick Pt foil (99.99 % purity from Goodfellow) was surrounded by two 7 μm thick plates of amorphous Al_2O_3 produced by physical vapor deposition that served as both the pressure medium and thermal insulation. Al_2O_3 was used since the melting point (~2350 K at ambient pressure) is always higher than the melting point of Pt in the studied pressure range [24]. The DACs were closed and the pressure was adjusted to the desired pressure for each experimental run, the highest pressure run that was carried out was at 50 GPa based on the Pt equation of state reported by Fratanduono et al. [25]. Several heating cycles were carried out on each DAC, the number of which depended on the sample size used, with a fresh area of the sample exposed after any pressure changes. That is, for larger culet diameters, the sample size was typically larger to allow for multiple heating spots. For the ambient pressure experiments a 25 μm thick Pt foil was placed between two single crystal sapphire plates.

Optical setup

Upstream (US, towards the X-ray source; before the sample stack) and downstream (DS) optical microscope images, laser heating, and temperature measurements are achieved using geoHEAT 60 (AdlOptica) objectives. This laser-heating setup corresponds to the one described in Ref. [21]. The objectives image the sample with dielectric turning mirrors (Semrock, MGP01-650–1300) that are transparent to X-rays at the used X-ray energy and remain in the X-ray beam path during the simultaneous XPCI and XRD measurements. Laser heating in the continuous mode was performed using a Nd:YAG laser ($\lambda = 1072$ nm, 200 W, IPG Laser GmbH) in an on-axis geometry, i.e. parallel to the X-ray beam and the DAC's compression axis, using polarization controls to split the beam for US and DS heating and control power on the sample. Beam shapers (πShaper 6_6, AdlOptica) were used to modulate the laser spot size on the sample plane between 10 μm and 70 μm. While the πShaper allows for a nominally flat-top beam profile, the actual beam shape may vary (for instance a donut-like intensity maximum in the

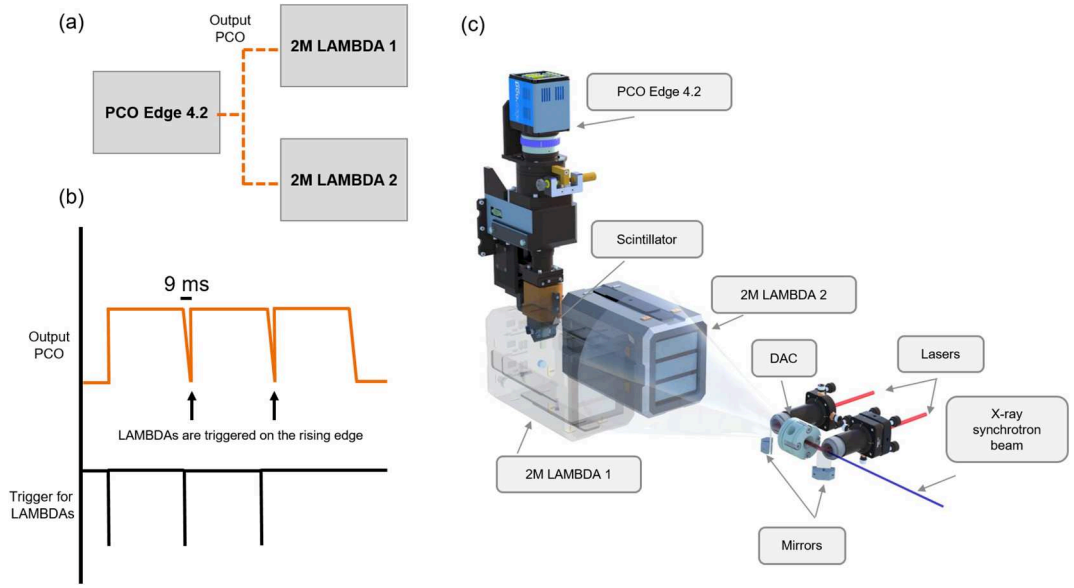

Fig. 1. Experimental setup. (a) + (b) show the triggering, whereas (c) shows a 3D drawing of the LH-XPCI-XRD setup. Note that the focal spot of the beam is upstream of the sample, so the sample is illuminated by the divergent beam.

beam profile). The US and DS laser power on the sample is controlled by the laser power and the angle of polarization rotators (one for DS and one for US) allowing for independent power input on each side of the sample.

US and DS thermal emission spectra were recorded simultaneously using the Andor Shamrock (SR-303i) spectrometer coupled with an Andor iStar 320T CCD (1024 × 256 pixels) intensified camera.

The vertical variation of the spectral signal on the iStar camera corresponds to vertical positions in the sample, allowing the determination of temperature variations across a hot spot. For spatial calibration, an image of a 5 μm pinhole was collected at the zeroth-order grating position, and a pseudo-Voigt function was fitted to the emission profile. The full width at half maximum (FWHM) of the fit indicates a conversion factor of 1.22 pixels per μm for both upstream and downstream imaging. This allows for the correlation of the observed thermal emission with corresponding XPCIdata. The signal is accumulated from a 12 μm wide area on the target. Data where the emission during laser heating was misaligned to the spectrometer were discarded. Where the thermal emission spectral signal was not horizontal in the detector, corrections to spectroradiometric analysis were performed using an in-house script.

Temperature determination

The transfer function of the laser heating optical system was determined using a calibrated tungsten halogen lamp (OPTEEMA Engineering GmbH, OL-245M-K3) at three different temperatures: 2200, 2500 and 2900 K. The tungsten wire was placed at the sample plane and imaged on the CCD and reference spectra were collected from the upstream and downstream sides separately. The reference spectra were then used in sample temperature determinations. Identical binning and image distortion corrections (see below) were applied to the emission data and reference images when determining temperature. From the reference data, the transmission function $T_f(\lambda,T)$, where T is the temperature, for a specific binning of the data was obtained, and applied to the emission data from the sample. A Planck-type fit in the grey-body approximation was used to determine the temperature.

LH-XPCI-XRD measurements

Coalignment of the X-rays and the optical images were made by comparing XPCI and optical microscope images. Temperature measurements were initiated at the start of the XPCI and XRD data collection, the laser was turned on during the runs after roughly 200 images of the pristine sample were acquired. The laser power was then ramped up manually during the experiment to produce gradually rising temperature and to optimize agreement of temperature on both sides of the sample using the independent rotators when double sided heating was used, which was the case in most experiments. Typically, the laser was turned off before the experiment ended. XPCI and XRD data were recorded with an exposure time of 100 ms and the corresponding thermal emission data were recorded with an acquisition time of 1 ms – 1 s (depending on the intensity). The time resolution of the temperature measurement was on the order of 1 s due to the readout time of the images. Over the time period of an experimental run (~2000 frames) typically between 50 and 100 emission spectra were collected. The emission spectra data were synchronized with the XRD and XPCI data after the experiment using timestamps within the machine precision.

Data analysis

In order to carry out the image analysis on the data, the contributions of the illumination (background) and the object have to be separated. This is achieved by a Principal Component Analysis (PCA) based dynamic illumination correction (in intensities). In contrast to our earlier work (Ref. [17]), where we utilized a correction for temporally instable illumination, which relied on the manual selection of parameters we have improved the scheme in two ways. First, we introduce a mathematical criterium to select the principal components and secondly, we employ a timely more accurate description of the instabilities in the illumination by subdividing the dataset into subsets for the PCA with a sliding window approach for the calculation of the principal components. The absolute sum of the weight distribution (ASW) for each principal component is utilized to determine whether the principal component is object-describing or background-describing, where we assume that for the former, the ASW is low and for the latter, the ASW is high. By applying a threshold, we can therefore automatically determine which principal components should be used to calculate the flat-field. The success of this approach was obtained without the need of any "reference" images, i.e. images without the DAC. The detailed procedure for the imaging analysis is explained in the SI with supporting Figs. S1–S6. It should be noted that this procedure can produce 'ghost'

features which appear as static artifacts in images associated with future or past sample changes (e.g. melting events) being included in the local components obtained from the sliding window, thus these can appear close to (but before) true melting; actual melting events can be discriminated from these sliding ghost features in that melting shows a clear dynamic, frame by frame change in appearance and in most cases a change in the raw images themselves.

For quick visualization of the XRD data, a new pipeline processing of XRD data, as described in Ref. [26] was also used to obtain, in near real time, batch view images of the XRD data. Pressure was determined from peak fits to the Pt (111) reflection using the Pt equation of state published in Ref. [25]. Pressures were obtained from XRD pattern(s) near the melting point P_{melt} and the uncertainty in pressure was estimated from the difference in pressure relative to the one at room temperature $dP = |P_{RT} - P_{melt}|$. The intensity plots of the XRD patterns are given in Figs. S7–S14 of the SI.

Melting temperature determination

Melting was assessed by observation of clear changes in the flat-field corrected images of the XPCI dataset which indicate the appearance of a new visible boundary in the sample. This boundary must be located in a region known to be associated (e.g. using radiographic information in raw images which is normally removed during PCA) with the sample of interest as well as within the spot where the laser is focused onto the sample. The onset of melting occurs just as the temperature is raised above the melting point of the sample, typically first visible only in a small region. The frame where this occurs is then compared with the temperature history for this run (Fig. 2). The maximum temperature in the sample at a corresponding time (on either side of the sample) is taken to correlate with the appearance of these features. We report two different temperatures in this study; T_{max} and T_{avg}. The former is a binning along the vertical axis of each emission strip in 2–5 pixels (2.44 μm–6.1 μm). Then the temperature is calculated in these respective binned regions and thereafter maximum temperature is selected. The latter refers to binning of 30–50 pixels (36.6 μm–61 μm) along the vertical axis in the emission strip around the emission maximum. More details on the temperature determination are given in the SI with Fig. S15. The melting temperatures T_{melt} (T_{max} and T_{avg}) were further obtained in one of two ways. If the $T(t)$ curve was continuous the closest temperature to the XPCI melt-frame was chosen with an uncertainty including the last temperature at which only solid was observed. However, several experimental runs showed a discontinuity in T around the melting point (see Fig. 2b). We attribute this jump in T to a change in emissivity between melt and solid. We note that initial melting can be observed before the temperature jump in some runs (see for instance Fig. 2(a)). To account for this effect, T_{melt} was, in these cases, chosen as the arithmetic average between the lower and the higher temperature with the uncertainty spanning this entire temperature range. Uncertainties in both cases were therefore estimated using the difference $dT = |T_{solid} - T_{melt}|$, with T_{solid} being the last temperature in which only the solid was observed in the XPCI as well as the error obtained from the fitting procedure for the temperature. In Figs. S16–S23 the temperature as a function of time is shown for all runs in this study.

Results and discussion

Representative still frames and movies (Supplementary material) generated from XPCI are shown in this section for ambient and high-pressure experimental runs. Our XPCI data unambiguously resolve melting and the XRD data in most cases confirms this. As a first test at benchmarking this technique we measured the melting temperature of Pt at ambient pressure since this temperature is well known (2041 K, see Fig. 3). For the ambient pressure run during laser-heating, a round feature suddenly appeared in the XPCI images, and sharply grew in size, having multiple concentric interference rings. Since sapphire remains solid at the onset of Pt melting ($T_{melt(sapphire)} = 2310$ K; molten in (c) in Fig. 3), we attribute this feature to the heated Pt foil, as no damage or movement of the sample was observed and the emission remained stable. The size of this feature agrees with the measured size of the heated region. Here, the temperature was found to be 2003(10) K, i.e. similar to the known melting temperature of Pt (2041 K) at these conditions (Fig. 3c). Also, there is an appearance of diffuse scattering originating from the liquid Pt in conjunction with the appearance of the multi-ring feature in XPCI. Therefore, we conclude that the circular features observed in the XPCI correspond to the edge of the melted region in the Pt sample. Since only the DS side was heated (showing a melting temperature of 2003(10) K), the US side was at a lower temperature (~1800 K). That is, the XPCI technique can directly resolve the phase boundary formation in Pt, despite the meager contrast in density for the liquid and solid phases of this metal during melting at ambient pressure.

Similar behavior of the Pt samples at high pressure was observed, allowing for detection of melting and ultimately the determination of the melting temperature (Fig. 4). Under high pressures, the morphology of the melted region tended to have a wider variability in shape and was much sharper, sometimes showing irregularities associated with sample features. Similarly, while detection of melting was typically still clear, it was often more difficult to firmly establish that detected features were

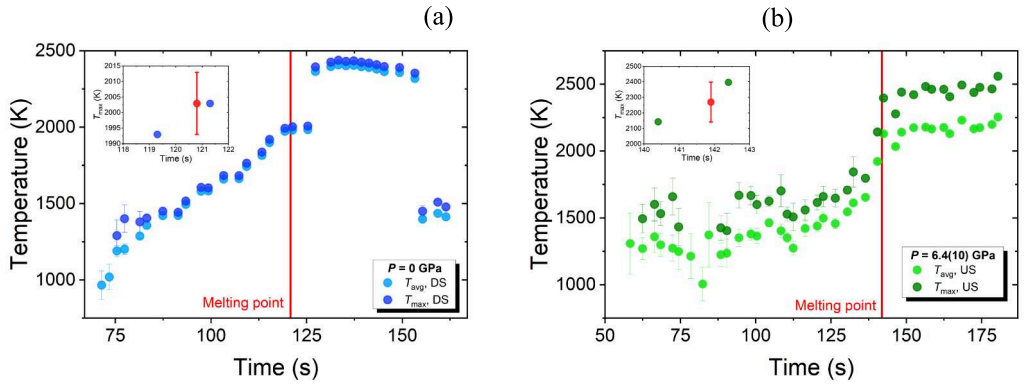

Fig. 2. T_{max} and T_{avg} as a function of time and spatial temperature gradients in the melt frame of Pt. Temperature either increases continuously (a) or shows a discontinuity (b) around the melt frame (marked by a red line); the former is an 'ideal run' whereas the latter is an extreme case of a difficult to interpret data set. For the first case (a), T_{melt} (red point in the inset) was chosen to be the closest temperature to the melt frame and the uncertainty estimated from the last temperature of the solid sample (see inset). Note that the melting happens before the jump in temperature. In the second case (b), to account for the discontinuity in $T(t)$, T_{melt} (red point in the inset) was chosen as the average of the lower and higher temperature with an uncertainty spanning this whole T-range. (For interpretation of the references to color in this figure legend, the reader is referred to the web version of this article.)

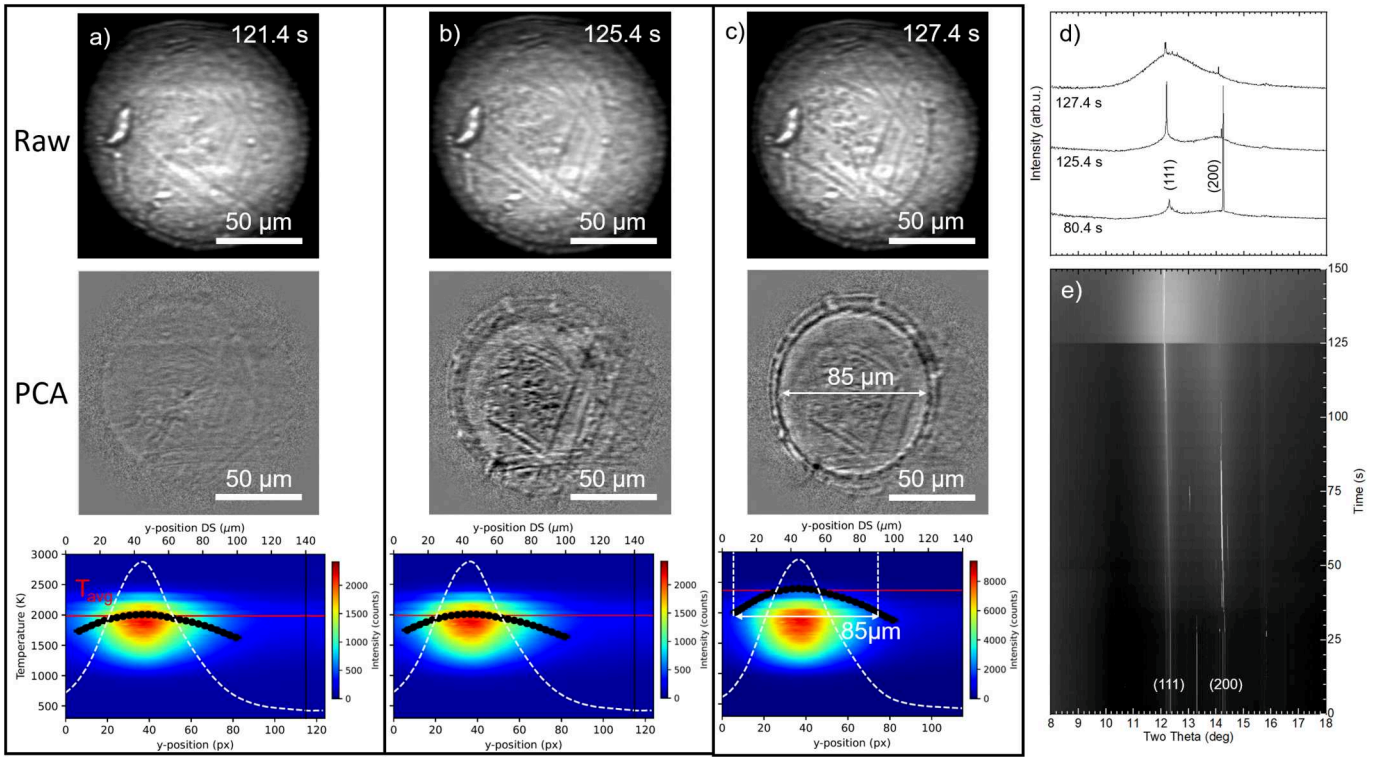

Fig. 3. Melting of Pt foil at ambient pressure during melting. The Pt foil was heated with an IR laser of ~25 µm beam diameter (FWHM) only from the downstream side until melting was observed. Data before (a) during (b) and after (c) melting occurred include raw XPCI images (top row), flatfield corrected equivalents using PCA (middle row), and associated temperature data (bottom row) including emission spectrograms (color maps), temperature gradients (black points), hot spot averaged temperature (red line), emission intensity distribution (white dashed line) for the downstream side. Additionally, the XRD data as a waterfall (d) and batch (e) plot show recrystallization before melting then appearance of strong diffuse scattering of the liquid in the XRD at ~125 s, precisely corresponding to appearance of the features identified as melting in XPCI. (For interpretation of the references to color in this figure legend, the reader is referred to the web version of this article.)

from the Pt foil melting. However, by using a pressure medium with a higher melting point than Pt, it ensures that the lowest detectable melting temperature is indeed from the Pt.

A PCA was a necessary step in the data processing in order to obtain high quality images which show changes in samples at high pressure. It should be noted that in a prior X-ray imaging study a PCA was not performed, therefore Fedotenko et al. in Ref. [10] may not have detected similar features in the high pressure melting of Pt.

In addtion, we note that due to the current configuration of the experiment, i.e. large X-ray beam that illuminates the entire sample compartment, the XRD data did not always provide clear evidence of melting (e.g. the disappearance of XRD peaks originating from solid Pt and the growth of a diffuse signal originating from the melted Pt). In many of the high-pressure runs, the scattering volume of the melt is very small compared to the diameter of the X-ray beam used for imaging. Moreover, there is also a large portion of the Pt sample that is not melted and likely close to room temperature. Therefore, we did not observe diffuse scattering from the melted Pt in these high-pressure runs. However, in all runs evidence of heating is observed in the XRD patterns. In some runs a discrete new peak grows in and shifts to lower 2θ which originated from the "hot" Pt, and in other runs the Pt reflections broaden towards lower scattering angle (2θ). Fig. 4f shows how the signal from hot Pt foil broadens the XRD peaks for Pt while the room temperature component loses some intensity but it does not shift in 2θ. Additionally, the presence of pressure gradients, and large changes during sample heating and partial annealing are tracked in XRD data and used to establish pressure uncertainty.

Fig. 5 reports our findings for the melting temperature versus pressure for Pt up to 50 GPa together with other published experimental and theoretical studies. Here, we provide the two temperatures of the melt, T_{max} and T_{avg}, as defined in the Materials and Method section. The values for these melting temperatures are also given in SI in Table S1.

It is common to fit the melting temperature to the Simon-Glatzel equation [33]:

$$T_{melt}(P) = T_{ref}\left(\frac{P - P_{ref}}{\alpha} + 1\right)^{\beta},$$

However, we found that β, in the Simon-Glatzel equation is close to 1, i.e. a linear function, within uncertainties. We therefore, fit our data using a linear function and report these fits to both T_{avg} and T_{max} establishing two distinct melt lines described by:

$$T_{melt}(P) = aP + T_0,$$

with fit parameters $a = 24.9(9)$ GPa^{-1} and $T_0 = 1981(10)$ K for T_{avg} and $a = 36.4(15)$ GPa^{-1} and $T_0 = 2003(19)$ K for T_{max}. These results can be directly correlated with what is expected for a Simon-Glatzel fit where β is fixed to 1, resulting in $\alpha = 80(3)$ GPa and $\alpha = 55(2)$ GPa for T_{avg} and T_{max}, respectively. However, we expect a flattening of the melting temperature curve at pressures above the highest achievable in this study which would not be captured by extrapolations of these linear fits or our Simon-Glatzel fits where β is fixed to 1. Therefore, extrapolations above 50 GPa should be made with caution.

While the difference (ΔT) between T_{avg} and T_{max} is negligible at lower temperatures and much less pronounced for a large laser beam, it becomes significant, however, at higher pressures and therefore higher temperatures (i.e. >2000 K) and reaches, in extreme cases, $\Delta T = 1{,}000$ K in one of the experiments (at the highest pressure). It is expected that the horizontal variation of temperature across the hot spot will result in similar differences. A fit utilizing peak temperature T_{max} in the sample as the condition for melting, shows good agreement with the study by Anzellini et al. [4] and by Errandonea [8] as well as the theoretical

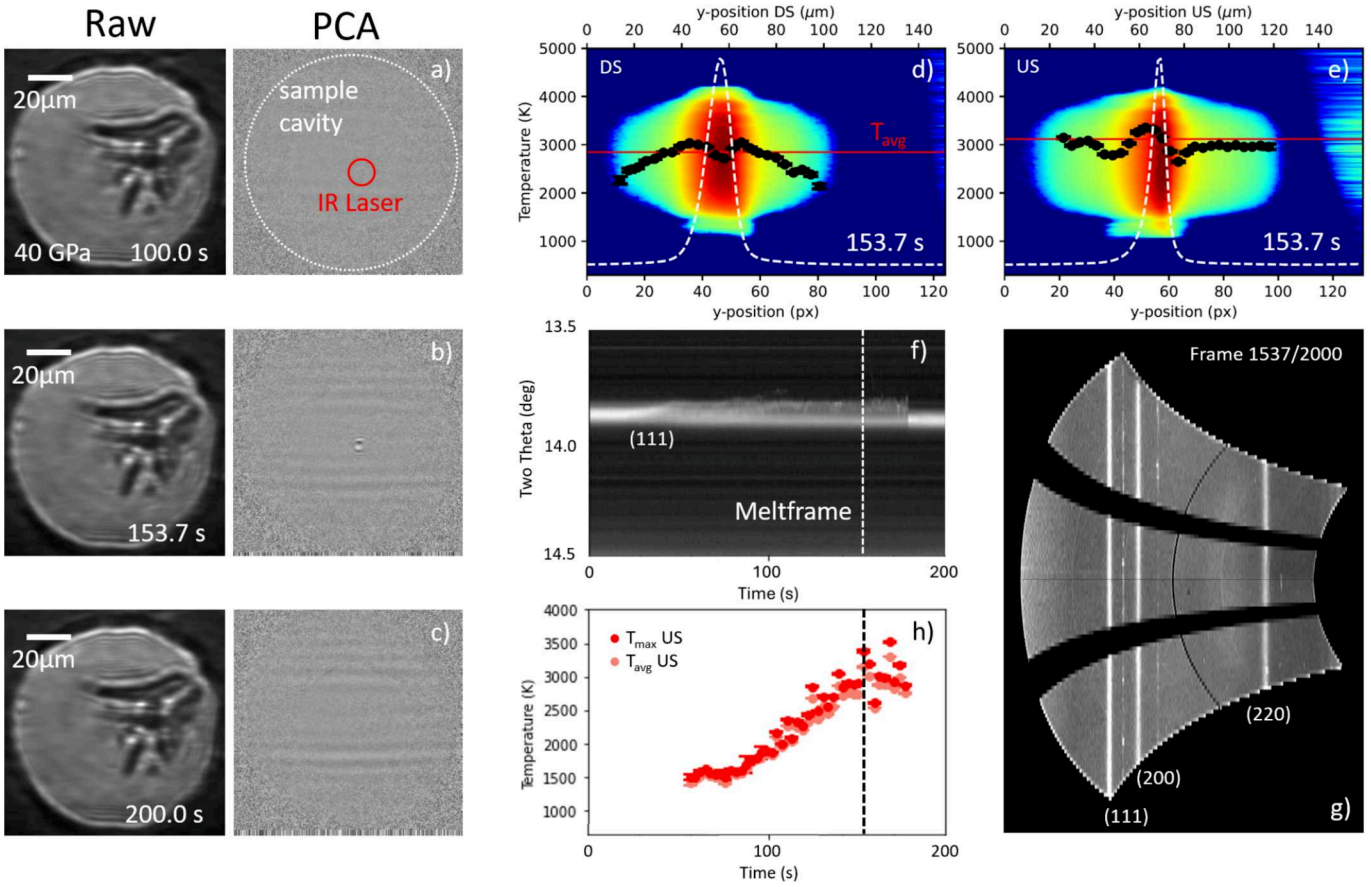

Fig. 4. Melting of Pt foil in Al_2O_3 at 42(2) GPa from double-sided laser heating. In this case, the entire cavity consists of three layers of uniform thickness, two amorphous Al_2O_3 plates (7 µm thick) surrounding a Pt layer (5 µm thick). Raw XPCI images and respective flatfield-corrected images using PCA before (a), during (b), and after (c) melting; the sample cavity and IR laser position are highlighted in (a). (d) Shows the spatial temperature variation. Note that the temperature is lower in the center compared to at the edge of the hot spot (see possible explanations in SI). The melting temperature was obtained from the maximum spatial temperature, observed on the upstream side (e); please note the temperature evolution during the experiment (h). XRD signal for the (1 1 1) reflection as a function of time is shown (f) together with the cake view of the XRD in the melt frame with Pt peaks labelled (g); other strong lines are due to the rhenium gasket.

studies by Belonoshko and Rosengren [31] and that by Zhang et al. [28]. In contrast, the fit of T_{avg} closely reproduces the studies by Kavner and Jeanloz [7] and that by Patel and Sunder [9]. While the study by Geballe et al. [5] is more scattered the fit to these values falls mostly in between our fits to T_{avg} and T_{max}. Interestingly, a recent ab initio study predicts a solid–solid transition from the face centered cubic structure to a randomly disordered hexagonal close-packed structure above ~40 GPa at high temperature via propagating stacking faults [32] as can be seen in Fig. 5 as the grey shaded area. This same transition was also predicted by *Z* methodology [34]. As discussed by Burakovsky et al. [32] the melt curve reported by Geballe et al. [5] virtually coincides with the predicted transition. We refer readers to [32] for a more complete comparison of the experimental work by Geballe et al. [5] and the *ab initio* results reported by [32]. However, a study to higher pressures as well as separate X-ray diffraction data, that does not have a large contribution of the cold sample, would be needed to confirm the hypothesis that Pt undergoes a pre-melting state where stacking faults propagate and create a random long-range order before melting [32].

While different methods are used to detect melting in the different studies, it is interesting to note that both Errandonea (Ref. [8]) and Patel and Sunder (Ref. [9]) use the speckle method, yet finding widely divergent temperatures with the cause of the discrepancy not understood. Using our measurement technique, our results agree with Errandonea [8] when we account for the temperature gradient in detail. However, when we do not include spatial variations in temperature in our analysis, and obtain an average value for the temperature from the hot spot, this agrees with Patel and Sunder [9]. Thus, the difference between the melting curves may not only relate to the accuracy of melting detection, but to differences in the quality of the associated temperature measurements and how the temperatures are extracted from these data. The magnitude of the systematic uncertainty resulting from temperature measurement approach here is similar to the range of melting temperatures seen across various datasets using different techniques in the past (Fig. 5) suggesting at least some degree of historic discrepancies can be attributed to the quality of temperature determination. While differences in detection method are likely to also contribute [2] this error should disappear for measurements which detect similar sample phenomena.

It seems evident that the large difference in melting temperatures (~2000 K at 100 GPa) between the various methods, therefore, can be partly explained by the difficulty and variability of characterizing temperature gradients in the sample. This observation might have been overlooked in earlier literature as the detection of melting temperature relied on larger-scale melting compared to the results obtained here, where melting can be detected already at a size of ~3 µm. Additionally, in contrast to prior studies using X-ray imaging in the DAC [10], where only bulk deformation of objects was available to identify melting, we can clearly detect phase transitions, allowing direct observation of phase boundaries within samples at the moment of melting. Similarly, in comparison to other methods reliant on sample movement to detect melting, such as the optical speckle method or fluctuation method, our technique is far more sensitive as no movement is required at all. Thus,

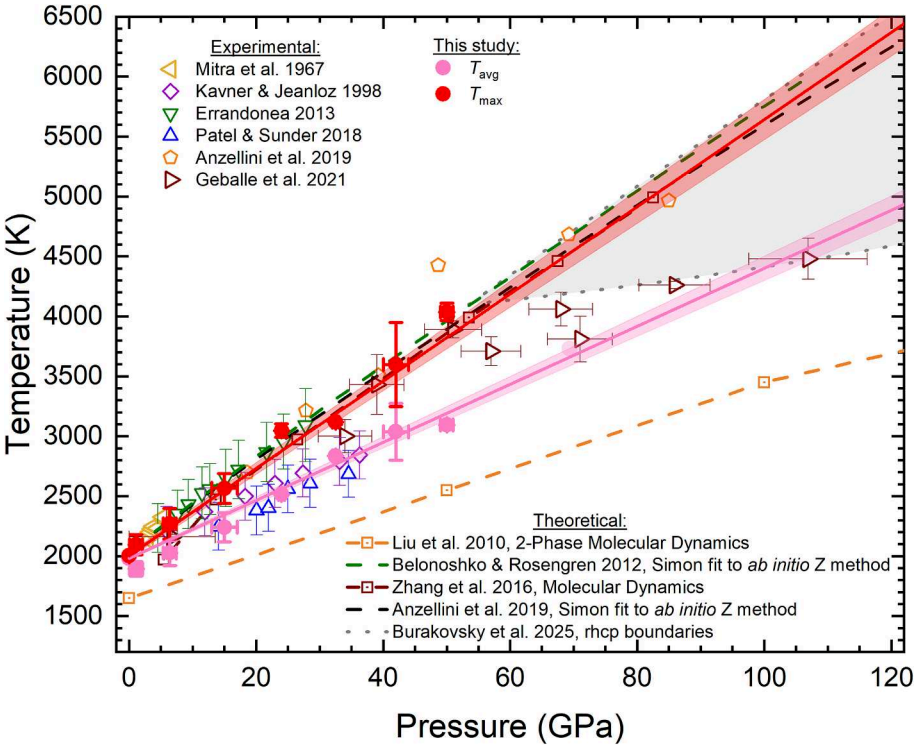

Fig. 5. Melting temperatures of Pt from this work including experimental literature [4,5,7–9,27] and theoretical studies [4,6,28–31]. The grey shaded area represents the predicted area of the randomly disordered hexagonal close-packed structure from Ref. [32]. The melting temperatures (T_{avg} and T_{max}) have been individually fitted to a linear function, $T_{melt}(P) = aP + T_0$, with $a = 24.9(9)$ GPa^{-1} and $T_0 = 1981(10)$ K for T_{avg} and $a = 36.4(15)$ GPa^{-1} and $T_0 = 2003(19)$ K for T_{max}. The lighter shaded areas of the fitted straight lines represent the 1σ bounds of the fits.

our measurement does not require any significant overheating of samples as might be necessary to initiate and detect large scale motion. Finally, the method developed here can potentially differentiate between recrystallization and melting for which the speckle method is less sensitive [3], and therefore can be applied to materials exhibiting strong recrystallization effects near melting points. This shows that the technique can be used to reproduce existing melt lines and establish unknown melt lines in the future.

Conclusion and outlook

A new experimental platform for direct X-ray phase contrast imaging of materials undergoing melting at high-pressure and high-temperature conditions in the laser-heated diamond anvil cell has been implemented at the laser heating experimental station of beamline P02.2, at PETRA III, DESY. This setup has expanded the temperature range over which simultaneous high-pressure XPCI and XRD experiments can be performed by employing laser-heating and is capable of detecting even small amounts of melt. With this new setup several new types of experiments can be fielded: 1) laser heating Earth relevant materials to temperatures relevant to the interior of the Earth and using a dynamic DAC to oscillate the sample at seismic frequencies, 2) the measurement of high-pressure viscosities of melts induced by laser heating by using particles with very high melting points and tracking their movement, or 3) the visualization of not just solid–liquid transitions but also solid–solid, liquid–solid, and demixing or mixing transitions in multi-phase materials.

Our results confirm a high melting temperature for Pt at high pressures, consistent with most current theoretical melting curves for Pt. Our findings also lend insight into prior discrepancies between experimental studies, showing that systematic errors in temperature originating in different measurement approaches can account for much of the spread in literature experimental data as well as reduced values compared to theoretical predictions. We note that improvements of the temperature determination can be made by incorporating a method of two-dimensional mapping the temperature distribution (both horizontally and vertically) within the sample chamber, such as by the peak scaling method [35], enabling a direct correlation of the imaging data to the temperature distribution. Therefore, this is planned as a future implementation at the P02.2 beamline. In addition, an implementation of a pink beam will enable the use of two different X-ray wavelengths, by utilizing different higher-order harmonics. This would result in the possibility of focusing to two different focal points: a larger one for imaging and a smaller one for XRD, which will enable precise local scattering from XRD within the laser heated area in conjunction with full sample imaging [36]. As the technical aspects of this novel technique continue to improve, we expect that the technique will further evolve into a state-of-the-art procedure for conducting melt studies at extreme pressures.

CRediT authorship contribution statement

Emma Ehrenreich-Petersen: Writing – review & editing, Writing – original draft, Visualization, Validation, Methodology, Investigation, Formal analysis, Data curation, Conceptualization. **Bernhard Massani:** Writing – review & editing, Writing – original draft, Visualization, Validation, Software, Methodology, Investigation, Formal analysis. **Thea Engler:** Writing – review & editing, Visualization, Validation, Software, Methodology, Investigation, Formal analysis. **Olivia S. Pardo:** Writing – review & editing, Validation, Investigation. **Konstantin Glazyrin:** Writing – review & editing, Resources, Methodology, Investigation. **Nico Giordano:** Writing – review & editing, Resources, Investigation. **Johannes Hagemann:** Writing – review & editing, Validation, Supervision, Software, Methodology, Conceptualization. **Daniel Sneed:** Writing – review & editing, Investigation. **Timofey Fedotenko:** Writing – review & editing, Resources, Methodology. **Daniel J.**

Campbell: Writing – review & editing, Investigation. **Mario Wendt:** Resources, Methodology. **Sergej Wenz:** Resources, Methodology. **Christian G. Schroer:** Writing – review & editing, Supervision, Funding acquisition. **Mathias Trabs:** Writing – review & editing, Supervision, Funding acquisition. **R.Stewart McWilliams:** Writing – review & editing, Supervision, Resources, Investigation, Funding acquisition. **Hanns-Peter Liermann:** Writing – review & editing, Supervision, Resources, Project administration, Methodology, Funding acquisition, Conceptualization. **Zsolt Jenei:** Writing – review & editing, Supervision, Resources, Project administration, Methodology, Funding acquisition, Data curation, Conceptualization. **Earl F. O'Bannon:** Writing – review & editing, Validation, Supervision, Resources, Project administration, Methodology, Investigation, Funding acquisition, Formal analysis, Conceptualization.

Declaration of competing interest

The authors declare that they have no known competing financial interests or personal relationships that could have appeared to influence the work reported in this paper.

Acknowledgements

We acknowledge DESY (Hamburg, Germany), a member of the Helmholtz Association HGF, for the provision of experimental facilities. Parts of this research were carried out at PETRA III. Beamtime was allocated under long term project proposals II-20211051, and II-20230680. Portions of this work were performed under the auspices of the U.S. Department of Energy by Lawrence Livermore National Laboratory under Contract No. DE-AC52-07NA27344. This result is part of a project that has received funding from the European Research Council (ERC) under the European Union's Horizon 2020 research and innovation programme (Grant agreement No. 101002868). Helmholtz Association (HIDSS-0002 (DASHH)) is greatly acknowledged. This research was supported in part through the Maxwell computational resources operated at DESY. This research was supported by Hi-Acts, an innovation platform under the grant of the Helmholtz Association HGF. „Bundesministerium für Bildung und Forschung" under contracts 05KS7RF1, 05K10RFA and 05K13RF1 in the frame work of the Verbundforschung "Verbundprojekt: Messeinrichtungen für die Material- und Strukturforschung an PETRA III, Teilprojekt 2: Laserheizung für die 'Extreme Conditions'-Station" (PI.: B. Winkler, Uni. Frankfurt) is greatly acknowledged.

In addition, we want to thank Guillaume Morard for supplying the amorphous Al_2O_3 plates and Karen Appel for cutting of Al_2O_3 disks. Lastly, we want to thank Zena Younes for help during the beamtimes.

Appendix A. Supplementary data

Supplementary data to this article can be found online at https://doi.org/10.1016/j.rinp.2025.108132.

Data availability

Data will be made available on request.

References

[1] Morard G, Boccato S, Rosa AD, Anzellini S, Miozzi F, Henry L, et al. Solving controversies on the iron phase diagram under high pressure. Geophys Res Lett 2018;45(11). https://doi.org/10.1029/2018GL079950. pp. 11–74,82.
[2] Sinmyo R, Hirose K, Ohishi Y. Melting curve of iron to 290 GPa determined in a resistance-heated diamond-anvil cell. Earth Planet Sci Lett 2019;510:45–52. https://doi.org/10.1016/j.epsl.2019.01.006.
[3] Anzellini S, Dewaele A, Mezouar M, Loubeyre P, Morard G. Melting of iron at earth's inner core boundary based on fast X-ray diffraction. Science 2013;340:464–6. https://doi.org/10.1126/science.1233514.
[4] Anzellini S, Monteseguro V, Bandiello E, Dewaele A, Burakovsky L, Errandonea D. In situ characterization of the high pressure – high temperature melting curve of platinum. Sci Rep 2019;9:13034. https://doi.org/10.1038/s41598-019-49676-y.
[5] Geballe ZM, Holtgrewe N, Karandikar A, Greenberg E, Prakapenka VB, Goncharov AF. Latent heat method to detect melting and freezing of metals at megabar pressures. Phys Rev Mater 2021;5:33803. https://doi.org/10.1103/PhysRevMaterials.5.033803.
[6] Liu Z-L, Yang J-H, Zhao Z-G, Cai L-C, Jing F-Q. The anisotropy of shock-induced melting of Pt observed in molecular dynamics simulations. Phys Lett A 2010;374:1579–84. https://doi.org/10.1016/j.physleta.2010.01.063.
[7] Kavner A, Jeanloz R. High-pressure melting curve of platinum. J Appl Phys 1998;83:7553–9. https://doi.org/10.1063/1.367520.
[8] Errandonea D. High-pressure melting curves of the transition metals Cu, Ni, Pd, and Pt. Phys Rev B 2013;87:54108. https://doi.org/10.1103/PhysRevB.87.054108.
[9] Patel NN, Sunder M. High pressure melting curve of platinum up to 35 GPa. AIP Conf Proc 2018;1942:30007. https://doi.org/10.1063/1.5028588.
[10] Fedotenko T, Dubrovinsky L, Aprilis G, Koemets E, Snigirev A, Snigireva I, et al. Laser heating setup for diamond anvil cells for in situ synchrotron and in house high and ultra-high pressure studies. Rev Sci Instrum 2019;90:104501. https://doi.org/10.1063/1.5117786.
[11] Boehler R, von Bargen N, Chopelas A. Melting, thermal expansion, and phase transitions of iron at high pressures. J Geophys Res Solid Earth 1990;95:21731–6. https://doi.org/10.1029/JB095iB13p21731.
[12] Schaeffer AMJ, Talmadge WB, Temple SR, Deemyad S. High pressure melting of lithium. Phys Rev Lett 2012;109:185702. https://doi.org/10.1103/PhysRevLett.109.185702.
[13] Karandikar A, Boehler R. Flash melting of tantalum in a diamond cell to 85 GPa. Phys Rev B 2016;93:54107. https://doi.org/10.1103/PhysRevB.93.054107.
[14] Boccato S, Torchio R, Kantor I, Morard G, Anzellini S, Giampaoli R, et al. The melting curve of nickel up to 100 GPa explored by XAS. J Geophys Res Solid Earth 2017;122:9921–30. https://doi.org/10.1002/2017JB014807.
[15] Dobrosavljevic VV, Zhang D, Sturhahn W, Chariton S, Prakapenka VB, Zhao J, et al. Melting and defect transitions in FeO up to pressures of Earth's core-mantle boundary. Nat Commun 2023;14:7336. https://doi.org/10.1038/s41467-023-43154-w.
[16] Hrubiak R, Meng Y, Shen G. Microstructures define melting of molybdenum at high pressures. Nat Commun 2017;8:14562. https://doi.org/10.1038/ncomms14562.
[17] Husband RJ, Hagemann J, O'Bannon EF, Liermann H-P, Glazyrin K, Sneed DT, et al. Simultaneous imaging and diffraction in the dynamic diamond anvil cell. Rev Sci Instrum 2022;93:53903. https://doi.org/10.1063/5.0084480.
[18] Liermann H-P, Konôpková Z, Morgenroth W, Glazyrin K, Bednarčik J, McBride EE, et al. The extreme conditions beamline P02.2 and the~extreme conditions science infrastructure at~PETRAIII. J Synchrotron Radiat 2015;22:908–24. https://doi.org/10.1107/S1600577515005937.
[19] Holmes NC, Moriarty JA, Gathers GR, Nellis WJ. The equation of state of platinum to 660 GPa (6.6 Mbar). J Appl Phys 1989;66:2962–7. https://doi.org/10.1063/1.344177.
[20] Santoro M, Lin J, Mao H, Hemley RJ. In situ high P-T Raman spectroscopy and laser heating of carbon dioxide. J Chem Phys 2004;121:2780–7. https://doi.org/10.1063/1.1758936.
[21] Konôpková Z, Morgenroth W, Husband R, Giordano N, Pakhomova A, Gutowski O, et al. Laser heating system at the extreme conditions beamline, P02.2, PETRA III. J Synchrotron Radiat 2021;28:1747–57. https://doi.org/10.1107/S1600577521009231.
[22] Bassett WA. The birth and development of laser heating in diamond anvil cells. Rev Sci Instrum 2001;72:1270–2. https://doi.org/10.1063/1.1343861.
[23] Boehler R. Laser heating in the diamond cell: techniques and applications. Hyperfine Interact 2000;128:307–21. https://doi.org/10.1023/A:1012648019016.
[24] Shen G, Lazor P. Measurement of melting temperatures of some minerals under lower mantle pressures. J Geophys Res Solid Earth 1995;100:17699–713. https://doi.org/10.1029/95JB01864.
[25] Fratanduono DE, Millot M, Braun DG, Ali SJ, Fernandez-Pañella A, Seagle CT, et al. Establishing gold and platinum standards to 1 terapascal using shockless compression. Science 2021;372:1063–8. https://doi.org/10.1126/science.abh0364.
[26] Karnevskiy M, Glazyrin K, Yu Y, Mondal A, Sanchez-Valle C, Marquardt H, et al. Automated pipeline processing X-ray diffraction data from dynamic compression experiments on the Extreme Conditions Beamline of PETRA~III. J Appl Crystallogr 2024;57. https://doi.org/10.1107/S1600576724004114.
[27] Mitra NR, Decker DL, Vanfleet HB. Melting curves of copper, silver, gold, and platinum to 70 kbar. Phys Rev 1967;161:613–7. https://doi.org/10.1103/PhysRev.161.613.
[28] Zhang B, Wang B, Liu Q. Melting curves of Cu, Pt, Pd and Au under high pressures. Int J Mod Phys B 2016;30:1650013. https://doi.org/10.1142/S0217979216500132.
[29] Wang P-P, Shao J-X, Cao Q-L. Melting properties of Pt and its transport coefficients in liquid states under high pressures. Int J Mod Phys B 2015;30:1550250. https://doi.org/10.1142/S0217979215502501.
[30] Jeong JW, Chang KJ. Molecular-dynamics simulations for the shock Hugoniot meltings of Cu, Pd and Pt. J Phys Condens Matter 1999;11:3799. https://doi.org/10.1088/0953-8984/11/19/302.
[31] Belonoshko AB, Rosengren A. High-pressure melting curve of platinum from ab initio Z method. Phys Rev B 2012;85:174104. https://doi.org/10.1103/PhysRevB.85.174104.

[32] Burakovsky L, Preston DL, Errandonea D. Ab initio study of randomly disordered hexagonal close-packed (rhcp) phase in platinum. J Appl Phys 2025;137:015109. https://doi.org/10.1063/5.0235811.
[33] Simon F, Glatzel G. Bemerkungen zur Schmelzdruckkurve. Z Für Anorg Allg Chem 1929;178:309–16. https://doi.org/10.1002/zaac.19291780123.
[34] Burakovsky L, Chen SP, Preston DL, Sheppard DG. Z methodology for phase diagram studies: platinum and tantalum as examples. J Phys Conf Ser 2014;500:162001. https://doi.org/10.1088/1742-6596/500/16/162001.
[35] Kunz M, Yan J, Cornell E, Domning EE, Yen CE, Doran A, et al. Implementation and application of the peak scaling method for temperature measurement in the laser heated diamond anvil cell. Rev Sci Instrum 2018;89:83903. https://doi.org/10.1063/1.5028276.
[36] Brown SB, Gleason AE, Galtier E, Higginbotham A, Arnold B, Fry A, et al. Direct imaging of ultrafast lattice dynamics. Sci Adv 2024;5:eaau8044. https://doi.org/10.1126/sciadv.aau8044.